Ultrafast Imaging of Laser Driven Shocks using Betatron X-rays from a Laser Wakefield Accelerator

Contact *jonathan.wood08@imperial.ac.uk*

J.C. Wood, N.C. Lopes[1], K. Poder, J.S.J. Bryant, J.M. Cole, Z. Najmudin and S.P.D. Mangles

The John Adams Institute, Imperial College London, United Kingdom

[1] also at GoLP/Centro de Fisica dos Plasmas, Instituto Superior Tecnico, Lisboa, Portugal

D. Chapman, D. Eakins, M. Rutherford, T. White

Institute of Shock Physics, Imperial College London, United Kingdom

E. Hill, S. Rose, M. Sherlock

Imperial College London, United Kingdom

K.T. Behm, K. Krushelnick, A.G.R. Thomas, Z. Zhao

University of Michigan, Ann Arbor, Michigan 48109-2099, United States

W. Schumaker, S. Glenzer

Stanford Linear Accelerator Center, Stanford University, Stanford, California 94309, United States

F. Albert, B.B. Pollock

Lawrence Livermore National Laboratory, Livermore, California 94550, United States

N. Booth, P. S. Foster, R. H. H. Scott

Central Laser Facility, STFC Rutherford Appleton Laboratory, Chilton, Didcot, OX11 0QX, United Kingdom

Introduction

Laser Wakefield Accelerators (LWFAs) have been intensively studied in recent years as a compact alternative to conventional accelerator technology. They have been shown to produce electron beams with energy spreads of a few percent [1,2,3] and electron beams are now routinely accelerated to 1 GeV in plasma lengths of approximately 1 cm [4,5,6]. This corresponds to an accelerating gradient one thousand times higher than found in a radio-frequency accelerator [7], which is one of the greatest advantages of this technology. LWFAs have also been demonstrated as sources of hard, bright x-rays [8], referred to as 'betatron radiation', with intensity high enough for single shot imaging. The x-ray beam produced is very broadband [9,10] with duration at the few fs level [11] which makes this a very interesting source for applications. The micron scale source size permits high resolution imaging in a compact geometry. In addition it means that propagation based phase contrast imaging of samples can be performed as has been demonstrated in Refs. [12,13]. Previous betatron imaging experiments have imaged only static objects [14,15] and therefore have not taken advantage of the ultrashort temporal nature of this source.

Here we present results from a proof of principle experiment on imaging laser driven shock waves in silicon, demonstrating that this source can be used to temporally resolve physics that would previously have required a considerably much larger and more expensive accelerator. Indeed a similar shock imaging experiment has recently been performed at the Linac Coherent Light Source x-ray free electron laser [18]. This work shows that the betatron radiation source has the potential to bring sub-surface shock physics measurements such as this down to the university laboratory scale.

Generation of Betatron Radiation

When a short ($c\tau < \lambda_p$), relativistically intense laser pulse propagates through a plasma it drives a nonlinear plasma oscillation in its wake, a 'wakefield'. For normalised vector potentials $a_0 > 4$ this wakefield takes the form of a single, almost spherical bubble that is completely devoid of electrons [16,17] with accelerating fields on the order of 100 GV/m. This regime can be reached using laser pulses with $a_0 < 4$ due to self-focussing and self-compression of the pulse within the plasma.

Electrons injected in to this bubble off-axis (or with transverse momentum) experience a linear restoring force towards the axis and oscillate within the bubble structure at the betatron frequency $\omega_\beta = \omega_p/\sqrt{(2\gamma_{e,z})}$, where ω_p is the nonrelativistic plasma frequency and $\gamma_{e,z}$ is the electron gamma factor in the longitudinal direction. These oscillations emit radiation which is frequency boosted in the lab frame by a factor of $2\gamma_{e,z}^2$, which is in the hard x-ray region of the spectrum for 100's MeV electrons. For typical experimental parameters used in LWFA experiments the undulator parameter $K = \gamma k_\beta r_\beta >> 1$ meaning that this radiation is broadband. k_β is the spatial frequency of betatron oscillations and r_β is the betatron oscillation radius. The spectrum of radiation is well approximated by the on-axis synchrotron spectrum [9,10] given in equation 1. The critical energy E_c is given in equation 2 and is the energy above and below which half of the energy in the angularly integrated spectrum is contained.

$$\frac{d^2I}{dEd\Omega} \approx N_\beta \frac{3e^2}{2\pi^3\hbar c\epsilon_0}\gamma_{e,z}^2\left(\frac{E}{2E_{crit}}\right)^2 \mathcal{K}_{2/3}^2\left(E/2E_{crit}\right) \qquad \text{Eq. 1}$$

$$E_c = \frac{3\hbar}{4c}\gamma_{e,z}^2\omega_p^2 r_\beta \qquad \text{Eq. 2}$$

Measured Properties of the Betatron Source

This x-ray source was characterised using the setup shown in Fig. 1. The drive laser was the Gemini South beam. (12.2 ± 0.3) J was delivered to the gas target in a 45 fs FWHM pulse, with a central wavelength of 800nm. An *f*/20 off-axis parabolic mirror was used to focus the pulse to a slightly elliptical FWHM spot size of 43 × 31 µm. Assuming that at most 50% of the energy was contained in the FWHM spot, the peak focussed intensity was $(2.6\pm0.6)\times10^{19}$ W/cm^2, corresponding to a peak a_0 of (3.5 ± 0.4). The pulse was focussed in to a 10 mm long gas cell. The plasma electron density could be varied by varying the backing pressure to the gas cell. For the best x-ray imaging conditions the plasma number density inside the cell was $n_e = 5\times10^{18}$ cm^{-3}.

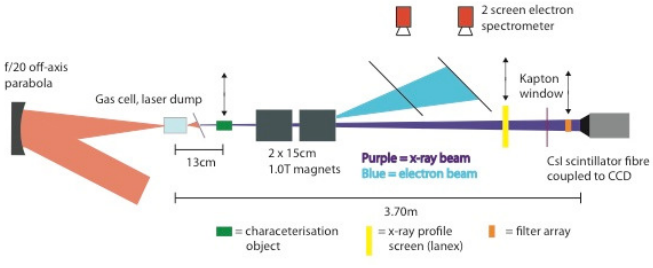

Figure 1: Diagram of the experimental setup used during the source characterisation.

Two 15 cm long 1.0 T dipole magnets were used to disperse the electron beam, which was recorded on two scintillating lanex screens. The typical energy of the high energy peak in the electron spectrum was approximately 700 MeV. Based on previous measurements at the same facility, the total charge in the beam above approximately 200 MeV was expected to be at the 100 pC level.

The x-ray beam spatial profile was measured using a scintillating lanex screen placed on the laser axis. The FWHM beam divergence was 20 mrad × 10 mrad in the vertical and horizontal planes respectively. The laser was vertically polarised, suggesting that the laser polarisation could be playing a role in determining the transverse momentum of the injected electrons.

The critical energy of the spectrum was estimated by detecting the transmission of the x-ray beam through an array of different metal filters with a caesium iodide scintillator that was fibre coupled to a 16-bit CCD. The estimated transmission for the set of filters was calculated for a range of critical energy values E_c', assuming an on-axis synchrotron spectrum. A least squared fit between these estimations and the data revealed the best estimate of the critical energy $E_{c,best}$ from the set E_c'. At the optimal imaging conditions (i.e. high flux, high resolution) we found $E_{c,best}$ = (25±5) keV, where the error given is the standard deviation calculated from multiple shots. Combining this with the peak electron energy and the plasma density in equation 2 gives an estimated source size $2r_\beta$ = 1.0 µm.

The x-ray camera has been previously calibrated so that total photon number could be calculated assuming a known spectrum. With a 25 keV critical energy spectrum and a 20 × 10 mrad beam profile (7 ± 3) × 10^9 photons were produced per shot with an energy above 1 keV. This corresponds to a peak brightness of 4×10^{23} photons/s/mm^2/mrad^2/0.1%BW, where the pulse length has been assumed to be 30 fs. The spectral flux that is inferred from the measurements outlined here is shown in Fig. 2.

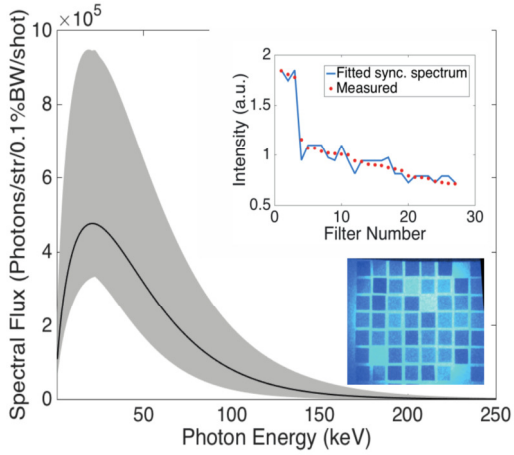

Figure 2: Peak spectral flux of the betatron source (black line). The grey region is the 1σ uncertainty in this measurement. Inset bottom left is a typical x-ray image of the filter array. Inset top right is a plot of the measured transmission through a number of the filters (red dots) compared to the best fit synchrotron spectrum (blue line).

The source size was independently verified by imaging the flat edge of a cleaved silicon crystal, to measure the line spread function of the system. In the case of a perfect detector this would be limited by the source size for this system. The image of this hard edge and the calculated line spread function are shown in Fig. 3. Clearly the scintillator/ camera combination is the major limitation of the resolution of our system. Comparing the measured modulation transfer function with that provided by the scintillator manufacturer suggests a source size of close to 1 µm, which is in good agreement with estimates based on the measured x-ray spectrum.

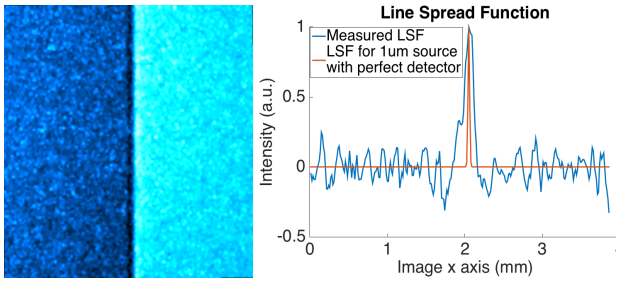

Figure 3: Left: X-ray image of the edge of a cleaved silicon crystal. Right: Line spread function of the imaging system deduced from the hard edge image (blue) and the expected line spread function produced by a 1.0µm source (red).

Shock Imaging Experimental Setup

To image shocks propagating in silicon the cleaved crystal was replaced by the silicon shock target. Two types of target were examined: a block of single crystal silicon 50 µm thick in the shock driver direction and 200 µm thick in the betatron probe direction, and a similar block with a 25 µm thick plastic tamper layer on the shock driver side. An *f*/2 off-axis parabolic mirror focused the uncompressed Gemini North beam on to the target as shown in Fig. 4. (15.7 ± 1.0) J was delivered to the target in 1.5 ns. The spatial intensity profile of this pulse is shown as an inset on Fig. 4. This shape was chosen to allow a single shot scan of intensity vs. resultant shock conditions. The shock driving beam applied a peak material pressure in the range approximately 10-20 GPa. The delay between the shock driver beam hitting the target and the betatron probe could be varied continuously between 0 and 12ns.

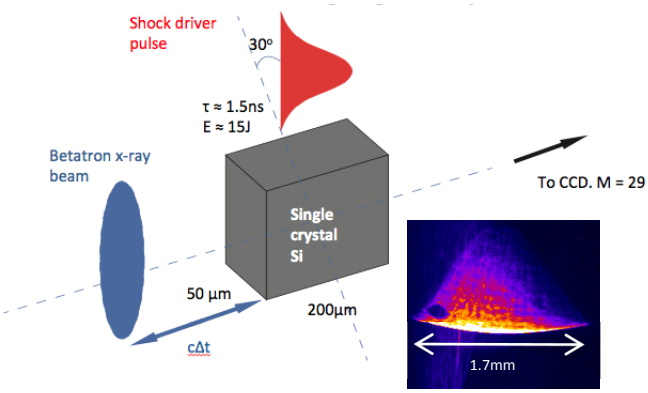

Figure 4: schematic of the shock interaction region. Inset bottom right is the shock driving laser beam profile at the shock surface.

Results

A time series of the propagation of the shock is displayed in Fig. 5 along with a plot of the apparent shock position as a function of time. This allows an estimation of the initial shock velocity of 5.9 km s^{-1}, which is consistent with the expected velocity of a plastic wave in silicon under these conditions. It is noted that the shock wave velocity is surprisingly linear for an unsupported shock. At the present time it is not clear why the elastic wave is not observed.

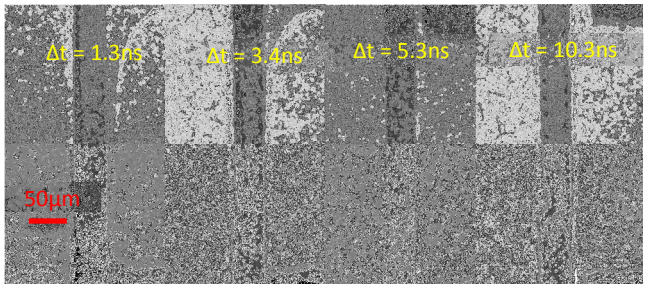

Figure 5: Above is a time series of the shock propagation in the untamped Si target. Right is a graph showing the shock propagation distance as a function of time (from different shots).

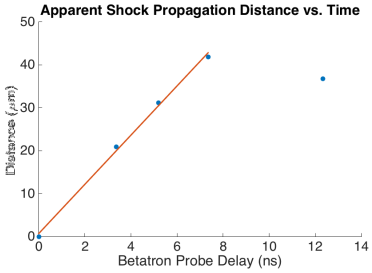

The shape of the shock wave closely followed the intensity profile of the driving laser pulse. A FLASH simulation was run in order to validate this somewhat complicated behaviour. The simulated material density corresponding to the first two images in Fig.5, i.e. shots at delays of 3.4 and 5.2 ns, is shown in Fig. 6. While this broadly mirrors the laser intensity profile once again there is a clear qualitative discrepancy between this and the images in Fig. 5. However it is important to note that the experimental images are a combination of absorption contrast and phase contrast images. Work is on-going to retrieve the electron density from these images using the transport of intensity equation [19,20,21].

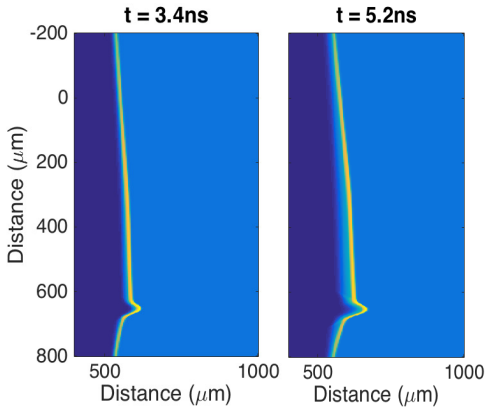

Figure 6: simulated material density 3.4 ns and 5.2 ns after the front of the shock driver pulse hits the surface of the silicon.

Finally, Fig. 7 shows a betatron x-ray image of a shocked, tamped silicon target. Tamper layers are commonly used to limit ablation of the shock target from the front surface, allowing for a smoother interaction with the driving laser. However their dynamics are not always well understood, simply because they are not seen. The partial spatial coherence of the betatron beam allows their dynamics to be recorded without sacrificing the high x-ray energies required to penetrate the higher atomic number shock samples. Figure 7 shows that a shock was driven in to the tamper layer even though the pressure applied by the laser was not unusually high. This shock in the tamper layer makes it very difficult to analyse the dynamics of the shock in the silicon, although it is very important to observe so that the results are not misinterpreted.

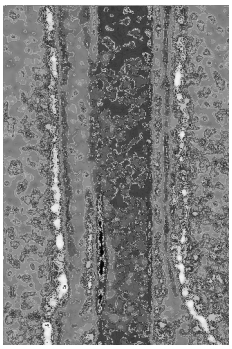

Figure 7: betatron x-ray image of a shocked silicon target with a 25 μm CH tamper layer. The sample was probed by the betatron radiation 4.4 ns after the shock driver started

Conclusions

This report has demonstrated that betatron x-rays from a Laser Wakefield Accelerator are suitable for the imaging of fast processes occurring in solid density material. Measurements of the x-rays indicated that their spectral flux was described by a synchrotron spectrum with critical energy (25±5) keV and that they came from a micron sized source. $(7\pm3)\times10^{9}$ photons were produced per shot and the narrow FHWM divergence of the beam at 20 × 10 mrad meant that single shot x-ray images could be taken at high magnification. These properties, added to the femtosecond nature of this x-ray source, make it a promising technology for imaging rapidly evolving phenomena at high resolution. This work shows the potential of this short pulse x-ray source by demonstrating that still images could be taken of a shock travelling at close to 6 km s^{-1}.

Acknowledgements

The author would like to thank the laser and engineering staff at the Central Laser Facility

References

1. S. P. D Mangles, C. D. Murphy, Z. Najmudin, A. G. R. Thomas et al., Nature **431**, 535–538 (2004).
2. C. G. R. Geddes, C. Toth, J. Van Tilborg et al., Nature **431**, 538–541 (2004).
3. J. Faure, Y. Glinec, A. Pukhov, S. Kiselev et al., Nature **431**, 541–544 (2004).
4. S. Kneip, S. Nagel, S. Martins, S. Mangles et al., Phys. Rev. Lett. **103,** 035002 (2009).
5. Nasr A. M. Hafz, Tae Moon Jeong, Il Woo Choi, Seong Ku Lee, Ki Hong Pae et al., Nature Photon. **2**(9), 571 (2008).
6. C. E. Clayton, J. E. Ralph, F. Albert et al., Phys. Rev. Lett. **105**(10), 105003 (2010).
7. M. Aicheler, P. Burrows, M. Draper, T. Garvey, P. Lebrun, K. Peach, N. Phinney, H. Schmickler, D. Schulte, and N. Toge. A Multi-TeV Linear Collider based on CLIC Technology: CLIC Conceptual Design Report. Technical report, 2012.
8. S. Kneip, C. McGuffey, J. L. Martins, S. F. Martins et al., Nature Phys. **6**(12), 980–983 (2010).
9. E. Esarey, B. Shadwick, P. Catravas, and W. Leemans. Phys. Rev. E **65**(5), 056505 (2002).
10. S Fourmaux, S Corde, K Ta Phuoc, P M Leguay, S Payeur, P Lassonde et al., New J. Phys. **13**(3), 033017 (2011).

11. O. Lundh, J. Lim, C. Rechatin et al., Nature Physics. **7**(3), 219–222 (2011).

12. S. Fourmaux, S. Corde, K Ta Phuoc, P. Lassonde et al., Opt. Lett. **36**(13), 2426-2428 (2011).

13. S. Kneip, C. McGuffey, F. Dollar, M. S. Bloom, V. Chvykov et al., Appl. Phys. Lett. **99**, 093701 (2011).

14. S. Kneip, C. McGuffey, F. Dollar et al., Appl. Phys. Lett. **99**(9), 093701 (2011).

15. J. M Cole, J.C. Wood, N.C. Lopes, K. Poder et al., Sci. Rep. **5**, 13244 (2015).

16. A. Pukhov and J. Meyer-ter Vehn. Appl. Phys. B: Lasers and Optics **74**(4-5), 355–361, (2002).

17. W. Lu, C. Huang, M. Zhou, W. B. Mori, T. Katsouleas. Phys. Rev. Lett. **96**(16), 165002 (2006).

18. A. Schropp et al., Sci. Rep. **5**, 11089 (2015).

19. A. Burvall et al., Opt. Express **19**, 10359 (2011).

20. D. Paganin et al., Journal of Microscopy **206**, 33-40 (2002).

21. G. R. Myers et al, Phys. Rev. A **76**, 045804 (2007).